Quantifying Temperature Changes in Tissue-Mimicking Fluid Phantoms using Optical Coherence Tomography and Envelope Statistics

Subaagari Seevaratnam[a], Amitpal Bains[a], Mashal Farid[a], Golnaz Farhat[b,c], Michael Kolios[a], Beau A. Standish[a]

[a]Dept. of Electrical and Computer Engineering, Ryerson University, 350 Victoria Street, Toronto, ON, CAN M5B 2K3;
[b]Dept. of Medical Biophysics, University of Toronto, 610 University Ave., Toronto, ON, CAN M5G 2M9;
[c]Imaging Research, Sunnybrook Health Sciences Centre, 2075 Bayview Ave., Toronto, ON, CAN M4N 3M5

ABSTRACT

Several therapies make use of a hypo or hyperthermia tissue environment to induce cell death in both benign and malignant tumors. Current progression in optical technologies, such as optical coherence tomography (OCT) and fiber Bragg gratings (FBG) sensors, could potentially provide viable information to explore the response of tissue when these temperature induced treatments are implemented. Studies were conducted with tissue-mimicking phantoms fabricated with polystyrene microspheres and glycerin to observe any relationship between the pixel intensities of the OCT images and their concurring envelope statistics. OCT images of the monitored region of interest were taken at 5°C intervals from 25°C to 60°C. Four probability distribution functions (PDF), Rician, Rayleigh, Normal and Generalized Gamma were used to investigate OCT envelope statistics as the temperature was altered. Using the Kolmogrov-Smirnov goodness of fit test, it was determined that the Generalized Gamma was the best fit. The scaling and shape parameters associated with the Generalized Gamma PDF were used to quantify the OCT envelope data to identify temperature changes within the tissue mimicking media. The Generalized Gamma PDF was verified as the best fit based on the Kolmogorov-Smirnov (K-S) test correlation factor being less than 0.05 ($p = 0.0158$). In addition to the PDFs, the OCT speckle decorrelation at varying temperature were also measured and quantified to detect the microspheres response to temperature changes. Initial results are very promising with future research focused on extending this methodology to monitor relative temperature changes in tissue during therapy. Clinical utility can be achieved if these optical techniques are used to evaluate the temperature-derived biological response of tissue and provide a feedback mechanism to improve procedural efficiency.

Keywords: optical coherence tomography (OCT), fiber Bragg grating (FBG), probability distribution function (PDF), autocorrelation, decorrelation time constant, envelope statistics, temperature

1. INTRODUCTION

Ablation is a clinical procedure that eliminates abnormal tissue caused by heart ailments, vasculature damage and cancer. Distinct ablation modalities that are being practiced today utilize extreme thermal conditions (with reference to body temperature) to ablate cancerous tissue, including: high intensity focused ultrasound ablation, radiofrequency ablation, cryoablation and interstitial laser ablation [1,2,3,4]. Cell lesions induced by hyper-thermal conditions are produced when the tissue temperature is increased within the range of 45°C - 56°C, which prompts thermal toxicity, protein denaturation and coagulative necrosis [1,2,3,4]. High intensity focused ultrasound (HIFU) ablation is a hyperthermia treatment that induces cell death by converting mechanical energy (sound waves) into thermal energy, which increases the temperature of the tumor tissue to 56°C [1,5]. HIFU treatments function within the frequency range of 0.8 – 3.5 MHz with significantly high energy levels that can be concentrated within a region of interest (ROI) [5]. Similarly, radiofrequency ablation (RFA) uses the same basic fundamentals of HIFU therapy, except radiofrequency energy is altered into heat through a needle electrode to ablate the target tumor at temperatures between 45°C - 50°C [2,5,6]. RFA often instill saline at the tip of the electrode to keep the cancerous region moist, which helps to target a larger volume of cancerous tissue [5]. Interstitial laser thermotherapy (ILT) also induces hyperthermia conditions by placing radioactive isotope grains in the ROI that are reactive to the laser light introduced by laser fibers (via image guidance) [3,5].

Contrary to hyper-thermal conditions, hypothermal incitation also instigates cell death with a process called cryoablation. Ablation of tissue occurs due to two reasons. The first is caused by cell injury from the formation of ice crystals and the

Optical Fibers and Sensors for Medical Diagnostics and Treatment Applications XIV, edited by Israel Gannot,
Proc. of SPIE Vol. 8938, 89380R · © 2014 SPIE · CCC code: 1605-7422/14/$18 · doi: 10.1117/12.2040161

preceding hyperosmotic extracellular conditions [5]. Secondly, the circulation system deteriorates due to endothelial damage in the vasculature [7]. The efficiency of the cryosurgery is dependent on the repetition of a freeze-thaw cycle, but clinical studies have exhibited that the minimum requirements to guarantee cell necrosis is two freeze-thaw cycles at a freezing temperature of -40°C, for a duration of three minutes [4,7].

To date, limited research has been performed on achieving localized measurements of the tissue response for these temperature-mediated therapies. Insight into these localized tissue responses could provide additional information to guide the therapies themselves. Advancements in optical coherence tomography (OCT) have provided a platform technology that could provide a cost-effective, minimally invasive and precise temperature feedback system for these hypo/hyperthermia-mediated treatments. OCT is an imaging modality that is appealing to multiple areas in clinical research due its capability of imaging microscopic structures (< 10 μm) non-invasively. The basic operation of the OCT is dependent on two components: an interferometer and a broadband light source. Structural images, approaching histological resolution, are acquired by measuring the backscattered photons of a sample and this provides information on the local reflectivity with respect to depth (generally in the range of 1-3 mm) of the tissue [8]. Speckle is an inherent feature in OCT images and carries information about particle interactions in a sample. This modulation pattern results from the light intensity measured from multiple scatterers within a concentrated scattering region of volume and varies according to the kinetics of the scatterers in the medium, which can be influenced by temperature. Observing statistical magnitudes of the OCT signal and the speckle decorrelation time constants of individual pixels, could provide additional information about the scatterers in the observed ROI, leading to a feedback mechanism for these temperature dependent therapies that are presented in this paper.

2. METHODOLOGY

2.1 Tissue-Mimicking Microsphere Phantom

A phantom with optical properties similar to biological tissue was created in order to observe the envelope statistics of the OCT signal with respect to temperature and to measure Brownian motion within the sample. The colloidal suspension phantom was fabricated with polystyrene microspheres (Polysciences, Warrington, PA) and glycerin USP (topical skin emollient), which is commonly used for pharmaceutical and cosmetic purposes. Glycerin USP, is a transparent and colorless aqueous solution with a glycerol content of over 95%, which has a refractive index of ~1.46 [9]. The monodisperse (uniform particle size) polystyrene microbeads, which behave like scatterers in the phantom had a mean diameter of 0.75 μm (with a standard deviation of 0.025 μm) and a refractive index of ~1.59 [10]. The resulting refractive index was calculated to be ~1.47. Figure 1 displays an image of phantom prior to the solution being mixed until it was homogeneous.

2.2 OCT/Temperature System

Once the phantom was thoroughly mixed, it was imaged using the Biophotonics and Bioengineering Laboratory's (BBL) in-house polygon swept-source OCT system with a central wavelength of 1310 nm at Ryerson University. As previously mentioned, the OCT system works on the basis of an interferometer, where light from a source is split between two pathways. One pathway reflects the photons from the phantom sample and the other reflects the photons from the reference arm. The combined light beams from the two arms produce an OCT fringe signal, due to the constructive or destructive addition of the propagating light waves. This information is then converted into a grey scale image (Thorlab Software via MATLAB). The OCT system had an A-scan rate of 72 kHz with a corresponding coherence length of 1.4 mm and an axial resolution of 6.9 μm in air. Figure 1 exhibits the combined temperature and imaging system. The phantom temperature was increased/decreased via a digital hotplate (Thermo Scientific ELED HP130910-33Q Cimarec), and the phantom temperature was monitored with a thermocouple (via multimeter). There were discrepancies between the feedback temperature from the hotplate and the thermocouple reading, and therefore required a calibration curve to compensate for the inconsistency of the hotplate feedback. Figure 1 also depicts the setup used for this experiment.

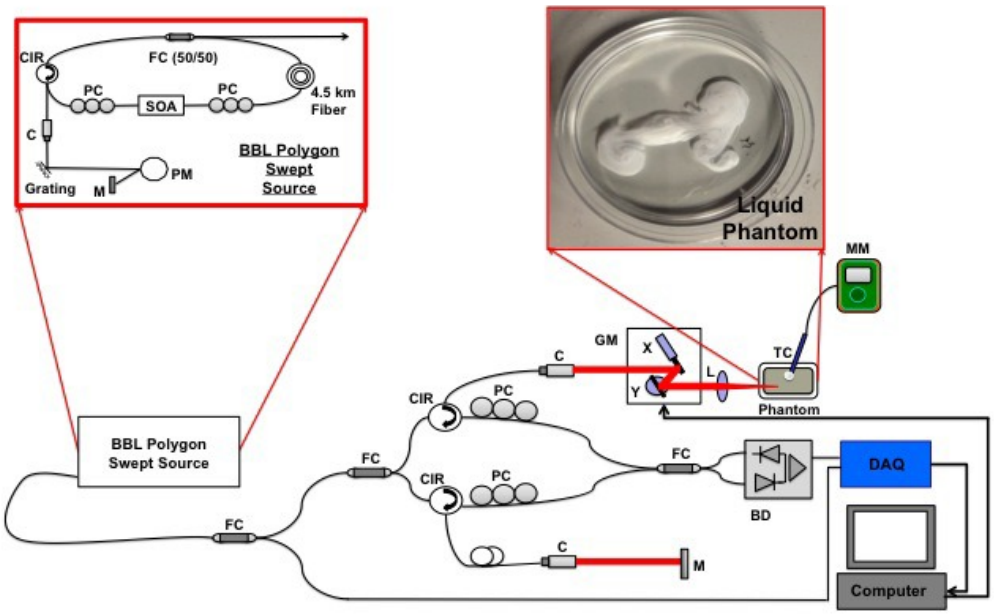

Figure 1. The Schematic of the temperature measurement and OCT systems; Circulator (CIR); Fiber Coupler (FC); Collimator (C); Balanced Detector (BD); Mirror (M); Polarization Controller (PC); Thermocouple (TC); Galvo Mirrors (GM); Lens (L); Multi-meter (MM); Polygon Mirror (PM); Semiconductor Optical Amplifier (SOA).

2.3 Envelope Statistics (Generalized Gamma)

The envelope statistics of OCT images have been previously studied for cell apoptosis detection and localized temperature quantification in tissue equivalent phantoms, where research has shown the best fit was the generalized gamma (GG) probability distribution [11,12] The goodness of fit was determined using the Kolmogorov-Smirnov (K-S) test. The K-S test evaluates a given distribution that follows a particular probability distribution function or compares two distributions and assesses whether they follow a specific probability distribution function. The equality between the comparisons is rated based on the correspondence between the empirical distribution and the theoretical cumulative distribution [13]. The GG probability distribution illustrates that the probabilities of the OCT intensities were highest in the first half of the backscatter intensity domain, and reveal a progressive decay in the second half of the speckle. The GG function is influenced by three parameters, which consist of two shape parameters 'v' and 'c' and a scale parameter denoted by 'a.' The GG function is represented by the following equation [12,14]:

$$f(x) = \frac{ac(ax)^{vc-1}e^{-(ax)^v}}{\Gamma(v)} \tag{1}$$

where, x represents the pixel intensity and $\Gamma(\cdot)$ represents the gamma function. The two-dimensional images acquired from the OCT system had the following dimensions: 3 mm × 3 mm (representation of the depth and transverse distances), and a user defined ROI that contained 1500 pixels. These pixels were then categorized into their respective backscatter intensities to produce a histogram dependent on the bins present in the ROI. OCT images were acquired at thermal settings of 22°C, 27°C, 31°C, 35°C, 40°C, 42°C, 47°C, 52°C and 57°C. Figure 2 shows a single-frame, which outlines the ROI for analyzing the envelope statistics of the OCT pixel intensities. The speckle that is portrayed in the OCT image is formed due to the polystyrene microbeads in the fluid phantom. It was our hypothesis that the speckle intensities within the ROI can change in accordance with the temperature fluctuations, and this relation can potentially help quantify the localized temperature in the ROI.

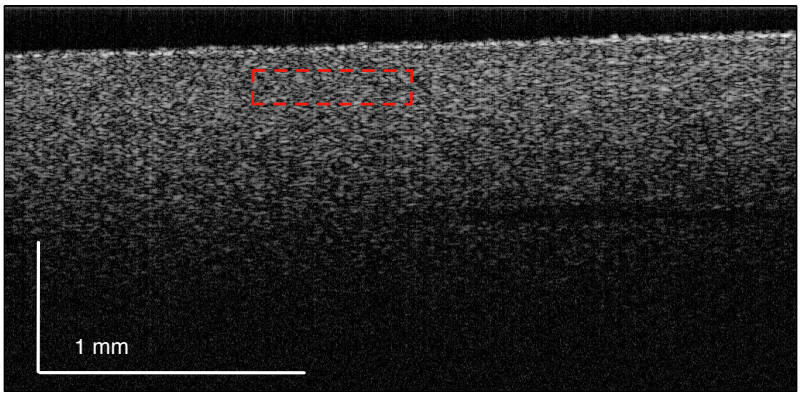

Figure 2. This a sample of a single frame 3 × 3 mm OCT image of the monodisperse (uniform particle size) microsphere phantom. The red dashed rectangle is the ROI that is being analyzed for the envelope statistics.

2.4 Measuring Brownian Motion of the Tissue-Mimicking Fluid Phantom

Brownian motion is the random movement of particles suspended within a fluid and this activity transpires due to the collisions between the particles and the molecules in the fluid [15]. Brownian motion can be measured using a light-scattering experiment, where a laser light beam is passed through a scattering medium and the reflected light is quantified using a detector [16]. In order to measure the decorrelation time of the monodisperse microsphere phantom, the speckle magnitude of one pixel was measured for duration of ten seconds, as the autocorrelation function is time-dependent. Similarly, the OCT system was used to acquire two-dimensional images, similar to the methodology used in envelope statistics (GG probability distribution function) but 180 frames were acquired at a frame rate of 18 Hz. An ROI of 100 pixels in the transverse direction and 45 pixels in the axial direction was chosen at a depth of 30 μm below the phantom surface. A pixel of interest was chosen within the ROI and its speckle intensity was noted from the collection of frames, and was plotted with respect to time (10 second duration). Figure 3 depicts the ROI and the pixel of interest of a single frame with its corresponding time signal, which looks similar to a noise signal.

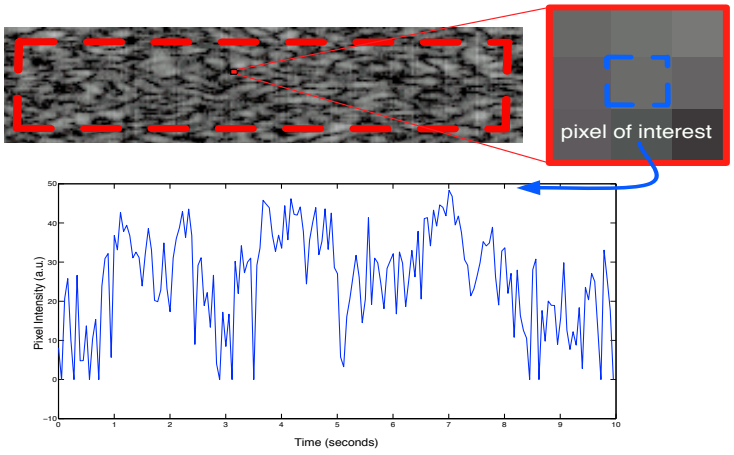

Figure 3. Red highlighted area is the ROI, where a single pixel is chosen to quantify the corresponding intensity in the acquired frames. The resulting signal looks like the noise signal illustrated above.

The autocorrelation function was obtained from the time-dependent intensity signal, via the inverse Fourier transform of the power spectrum signal. The autocorrelation function for a monodisperse microsphere phantom that experienced Brownian motion is represented by an exponentially decaying function, as seen in equation (2) [17]:

$$A(\tau) = e^{-2q^2 D_B t} \tag{2}$$

where, q is the wave vector notation, D_B is the diffusion coefficient, t is time and τ is the measured time constant (it is relevant to time). The wave vector coefficient and the diffusion coefficient are represented by the following equations, respectively [17]:

$$q = \frac{4\pi}{\lambda} \tag{3}$$

and

$$D_B = \frac{\kappa_B T}{6\pi\eta r} \tag{4}$$

where, λ is the wavelength of incident, κ_B is the Boltzmann's constant , T is the absolute temperature, η is the viscosity of the medium (glycerol) and r is the particle radius. The decorrelation time constant can be evaluated based on this function [17]:

$$\tau = \frac{1}{2q^2 D_B} \tag{5}$$

The decorrelation time can be evaluated by finding the exponential fit to the autocorrelation function, and from the exponential coefficient the decorrelation time can be determined. The results were verified with the theoretical model using equations (3), (4) and (5).

3. RESULTS AND DISCUSSION

3.1 Calibration of Hot Plate System

As previously mentioned, there were disparities between the sample temperature and the feedback provided by the hotplate. Therefore, a calibration curve was established with five experimental trials. For each trial, the hot plate was set at temperatures between 25°C - 80°C at 5°C increments and a digital thermocouple was used to take additional temperature measurements. The temperature calibration curve was created by taking the mean and the standard deviation of each temperature setting in all five trials. Figure 4 illustrates the results of the five trials and the resulting calibration curve.

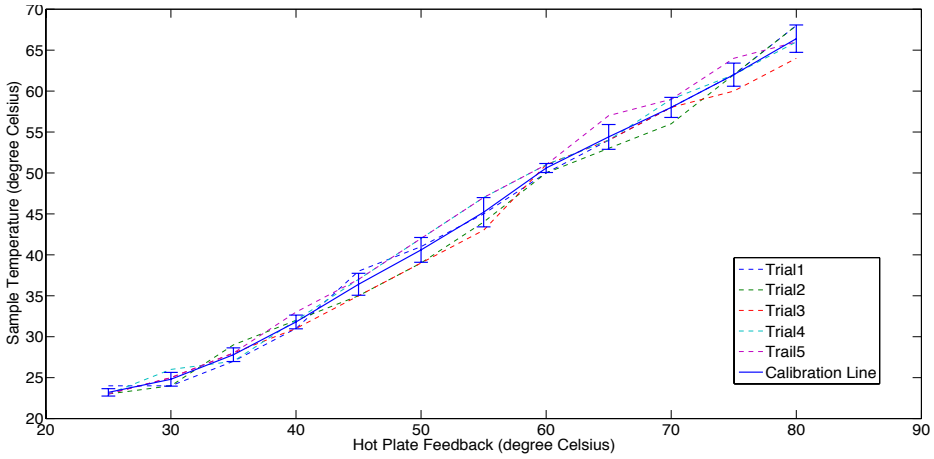

Figure 4. The calibration curve of the five trials sample temperature measurements with respect to the hot plate's feedback temperature. The error bars indicate the minimum and maximum deviation from the measured sample temperature using the thermocouple reading. The calibration curve is the resultant of the average of all five trial results.

The calibration curve shows a linear trend with respect to the hot plate temperature as shown by the equation:

$$T_S = 0.826 \times T_H + 0.0529 \quad (6)$$

where, T_S is the sample temperature and T_H is the hot plate temperature setting. The linear fit has a regression value of 0.9951, which indicates equation (6) correlates to the experimental data.

3.2 OCT Images and Envelope Statistics

Figure 5 exhibits the GG probability distributions for varying temperatures. The corresponding shape and scale parameters are illustrated in Figure 6. The values for shape parameter '*c*' are relatively stable with regards to the changes in temperature, except for a slightly higher peak at 31°C. The standard deviation amongst all the points was 0.1645, which signifies minimal changes in this shape parameter as the temperature was increased. The shape parameter '*c*' was fit with a linear function to check for significance via equation (7):

$$c = 0.0043 \times T_s + 1.7284 \quad (7)$$

where, c is the scaling parameter and T_S is the measured sample temperature. The slope of the linear function, shown in equation (7), demonstrates that parameter '*c*' is changing at a rate of 0.0043 /°C, which further indicates that it was minimally impacted by any temperature fluctuations. The function corresponded in a linear regression value of 0.111 that signifies a low correlation between the experimental data and its linear fit and these changes were therefore not statistically significant. Likewise, the shape parameter '*v*' also revealed no notable variance in the data, and also exhibited a low standard deviation of 0.1145. The linear fit of shape parameter '*v*', resulted in the following equation:

$$v = -0.0055 \times T_s + 1.2676 \quad (8)$$

where, v is the scaling parameter and T_S is the measured sample temperature. Similarly, the scale parameter '*v*' resulted in a descending small rate of change with respect to temperature as seen in of equation (8) with a linear regression of 0.366. The results show that the shape parameters had minimal impact from the temperature alterations. However, additional research is required to verify that the parameters '*c*' and '*v*' are marginally affected by temperature through the use of larger data sets. The relationship needs to be further studied by conducting more trials to see if this holds constant to all experiments of the same nature. The plot showing the ratio of the two shape parameters, '*c/v*', has the same orientation but is a scaled model of the shape parameter '*c*' plot, which also highlights that there is negligible deviance in the shape parameters.

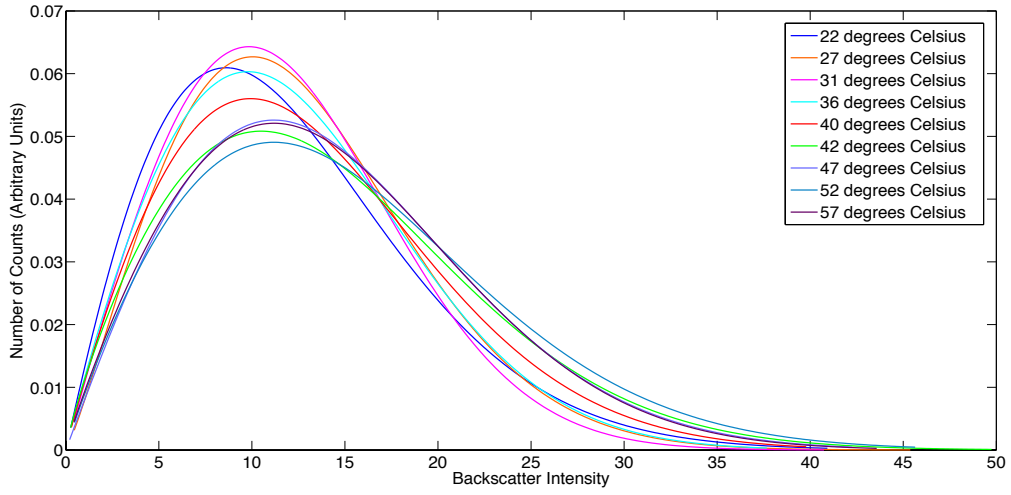

Figure 5. The GG probability distribution fits with respect to nine different sample temperatures. The plots reveal the varying shape and scales for the resulting probability distribution functions.

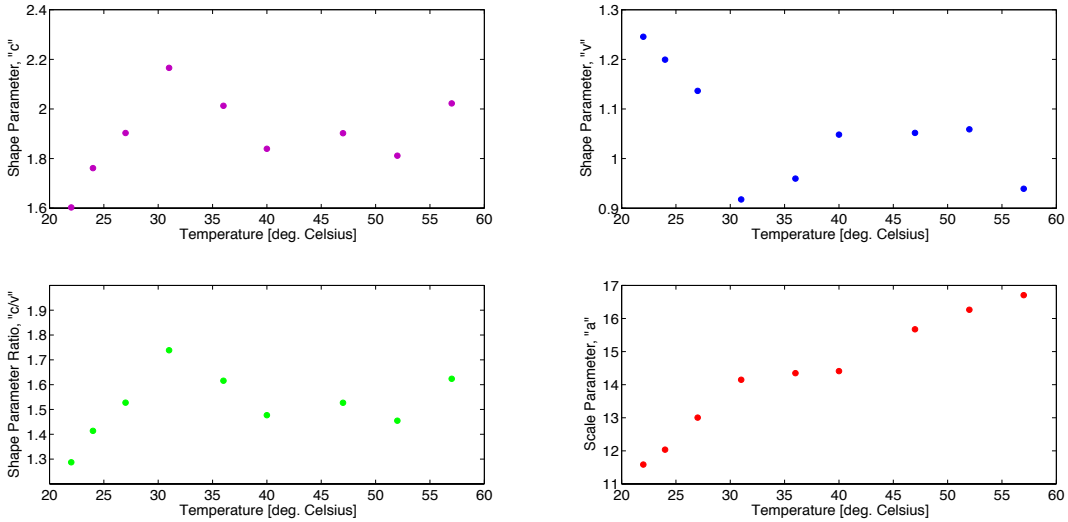

Figure 6. The three parameters of the GG probability function, were evaluated at temperatures between 22°C - 57°C; (a) shape parameter 'c', (b) shape parameter 'v', (c) shape parameter ratio and (d) scale parameter 'a'.

However, the scale parameter '*a*' did present something interesting, as there were noticeable changes in this parameter as the temperature was increased. There was a noticeable plateau in the parameter quantities within the sample temperature range of 30°C - 40°C, but the values still increased as demonstrated in Table 1.

Table 1. The 'c', 'v' and 'a' parameters results from the GG distribution fits with respect to temperature.

Sample Temperature	**Shape Parameter, 'c'**	**Shape Parameter, 'v'**	**Shape Parameter Ratio, 'c/v'**	**Scale Parameter, 'a'**
22	1.60308628	1.24570675	1.286888972	11.58558244
24	1.761330096	1.199519305	1.468363276	12.03425875
27	1.902795945	1.136540708	1.674199553	13.00433546
31	2.165826656	0.917682546	2.360104444	14.14874521
36	2.012804072	0.95966081	2.097411972	14.34817573
40	1.83972433	1.048325298	1.754917423	14.40837338
47	1.902348895	1.051711803	1.808811967	15.67281751
52	1.812009994	1.059014799	1.711033685	16.26308481
57	2.022470418	0.939209376	2.153375455	16.70370514

The scaling parameter '*a*' experimental data was fitted with a line of best fit, which yielded the following equation:

$$a = 0.1390 \times T_S + 9.0504 \tag{9}$$

where, a was the scaling parameter and T_S was the measured sample temperature and the scale parameter a vs. temperature is presented in Figure 7. The linear regression value of the line of best fit was 0.9506, which signifies a high correlation between the fit and the experimental data. A student t-test was performed to make an inference regarding the regression coefficients, and the resulting p-value was 7.93×10^{-6} (with a 5% significance level). This indicates the null hypothesis, which states that parameter '*a*' is not dependent on the sample temperature, can be rejected. The p-value demonstrates that the linear trend of the '*a*' parameter did not occur by coincidence and is statistically significant. The initial experimental trial affirms the scale parameter '*a*' is influenced by the modifications in temperature, whereas the shape parameters '*c*' and '*v*' do not vary to the same extent. More trials need to be conducted to verify whether this is a

suitable trend and holds true to other data sets, with different microsphere size along with translation to an *in situ* and ultimately the *in vivo* environment.

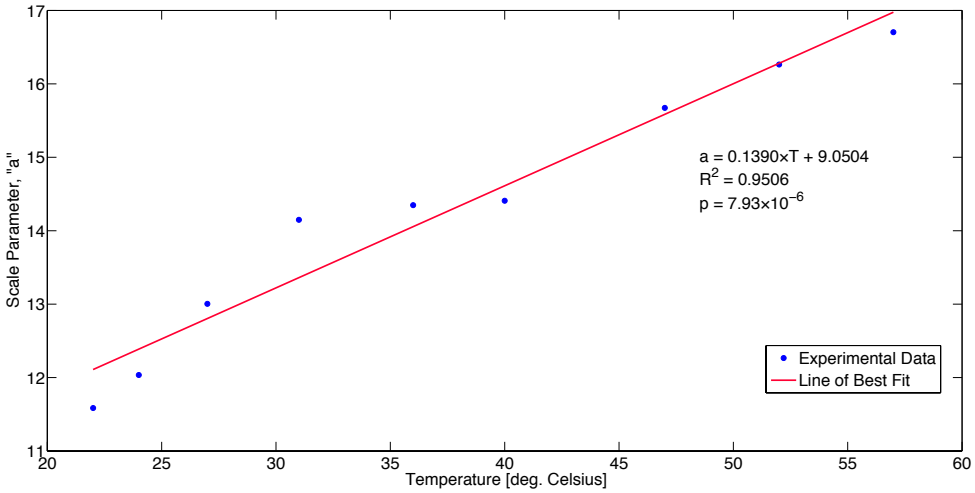

Figure 7. The scale parameter 'a' reveals a linear trend with respect to increasing temperature. The above graph shows the line of best fit with respect to the experimental data.

3.3 Brownian Motion and Decorrelation Time

Measuring the decorrelation time of monodisperse suspension fluid at varying temperature proved to be difficult with a 72 kHz OCT system (~18 Hz frame rate) imaging a transverse distance of 3 mm (1024 A-scans) because these settings provided a limited number of sample points to measure Brownian motion accurately. Figure 8 shows the intensity fluctuation of a single pixel in the defined ROI for duration of ten seconds at a temperature setting of 36°C. The decorrelation time of the scatterers generally measure a little over one second for temperatures greater than or equal to 25°C. Since there were only 18 samples (due to limited A-scan rate of system) to show swift changes occurring with the scatterers in the medium there was not enough information to fully investigate the effects of temperature on the OCT speckle decorrelation time. The imprecision in measuring the decorrelation time constant was not unique only for the temperature setting of 36°C, as it also posed limitations while measuring the time constants for other temperature settings. Despite the lack of samples the results are promising in the sense the general exponential decay shape is apparent in the autocorrelation function of the time-dependent intensity fluctuation signal, mentioned in equation (2).

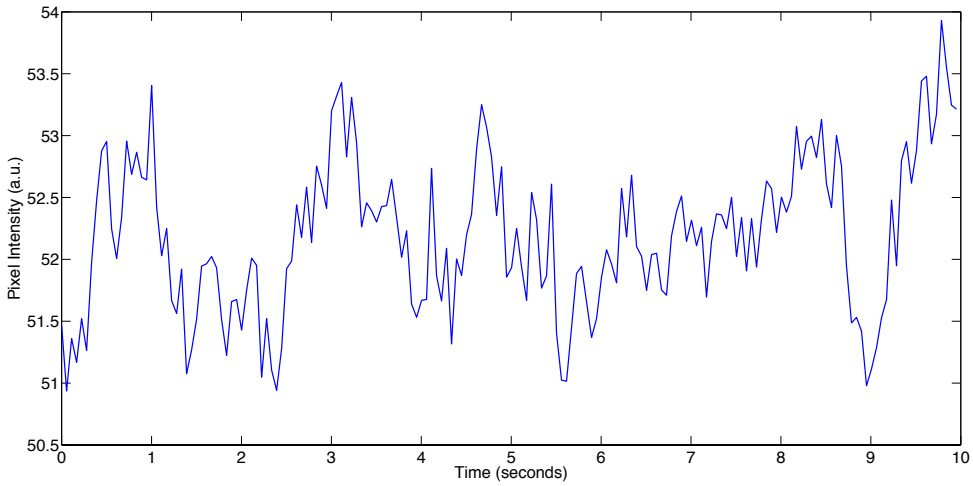

Figure 8. The intensity is measured as a function of time at 36°C; the signal's resemblance is similar to a noise signal.

Prior decorrelation studies conducted by Farhat et al. have successfully measured the decorrelation time constants with respect to different microbead sizes using a 166 Hz frame rate OCT system imaging a smaller transverse distance of approximately 0.4 mm (~ 64 A-scans), which provided a significant amount of samples to measure Brownian motion [17]. Figure 9 is the autocorrelation function of the intensity fluctuation signal, along with its line of best fit. In the case of Figure 9, the experimental data and the exponential fit match well at the temperature setting of 36°C, but this was not the case for all temperatures. This limitation can potentially be resolved by imaging a smaller field of view to increase the frame rate of the OCT system. The line of best fit provided the exponential constants, which allowed for the calculation of the time constant using equation (5). For the temperature trial at 36°C, the calculated decorrelation time constant was 246.4419 ms, which did not correspond to the theoretical quantity of 1.1453 seconds. Further experimentation is required with a higher frame rate OCT system to ensure that the decorrelation from Brownian motion could be quantified as we hypothesized.

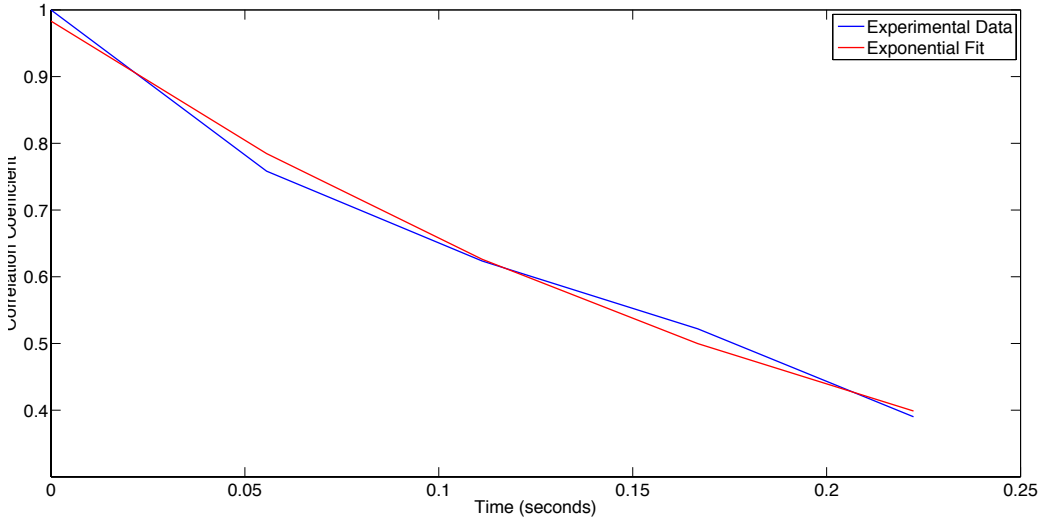

Figure 9. The autocorrelation function of the intensity time signal at a temperature setting of 36°C. The blue plot is the autocorrelation function from the experimental data, and the red plot is the exponential fit to determine the corresponding exponential constants.

4. CONCLUSION

Temperature oriented studies were conducted using the OCT imaging modality, and statistical analyses of the envelope statistics and autocorrelation function demonstrate the potential to measure temperature variations in tissue-mimicking fluid phantoms. From previous studies, it was concluded that the GG probability distribution function was the best fit for the OCT envelope statistics. The scaling parameter "*a*" of the GG PDF to the OCT images demonstrated a linear trend with respect to temperature, which was validated as statistically significant with the student t-test ($p<0.05$; $p = 7.93\times10^{-6}$). Measuring the decorrelation time did show changes with respect to temperature, but did not statistically correlate with the expected theoretical values. We believe repeating this study with an OCT system with an A-scan rate approaching a frame rate of 166 Hz, will provide the image speed to demonstrate the ability of OCT to monitor relative temperature changes in tissue-mimicking phantoms. This remains to be an active area of research at our laboratory, where this technique shows promise to provide direct measureable biological responses of tissue when exposed to temperatures imposed by hyper/hypothermal induced cancer therapies.

REFERENCES

[1] Kennedy, J. E., Ter Haar, G. R. and Cranston, D., "High intensity focused ultrasound: surgery of the future?" Br J Radiol 76(909), 590-599 (2003).

[2] Curley, S.A., Izzo, F., Delrio, P., Ellis, L. M., Granchi, J., Vallone, P., Fiore, F., Pignata, S., Daniele, B. and Cremona, F., "Radiofrequency Ablation of Unresectable Primary and Metastatic Hepatic Malignancies," Annals of Surgery 230(1), 1-8 (1999).
[3] Steger, A. C., Lees, W. R., Walmsley, K. and Bown, S. G., "Interstitial laser hyperthermia: a new approach to local destruction of tumours," Br Med J 299(6695), 362-365 (1989).
[4] Theodorescu, D., "Cancer Cryotherapy: Evolution and Biology," Rev Urol 6(Suppl.4) S9-S19 (2004).
[5] Kennedy, J. E., "High-intensity focused ultrasound in the treatment of solid tumours," Nature Reviews Cancer 5(), 321-327 (2005).
[6] Dupuy, D. E., Hong, R., Oliver, B. and Goldberg, S. N., "Radiofrequency Ablation of Spinal Tumors: Temperature Distribution in the Spinal Canal," American Journal of Roentgenology 175(5), 1263-1266 (2000).
[7] Chin, J. L., Lim, D. and Abdelhady, M., " Review of Primary and Salvage Cryoablation for Prostate Cancer," Cancer Control 14(3), 231-237 (2007).
[8] Standish, B. A., Lee, K. K. C., Jin, X., Mariampillai, A., Munce, N. R., Wood, M. F. G., Wilson, B. C., Vitkin, A. and Yang, V. X. D., " Interstitial Doppler Optical Coherence Tomography as a Local Tumor Necrosis Predictor in Photodynamic Therapy of Prostatic Carcinoma: An In vivo Study," Cancer Res 68(23), 9987-9995 (2008).
[9] DOW, [Origins of Some of the World's Most Consistently Pure Products… Synthetic Glycerine Products], The DOW Chemical Company, Michigan, Ontario, Mexico City and Horgen, 1-32 (1999).
[10] Kasarova, S. N., Sultanova, N. G., Ivanov, C. D. and Nikolov, I. D., "Analysis of the dispersion of optical plastic materials," Optical Materials 29(11), 1481-1490 (2007).
[11] Farhat, G., Yang, V. X. D., Czarnoto, G. J. and Kolios, M. C., "Detecting cell death with optical coherence tomography and envelope statistics," Journal of Biomedical Optics 16(2), 1-7 (2011).
[12] Seevaratnam, S., Farid, M., Farhat, G. and Standish, B. A., "Analyzing Effects of Temperature on Tissue Equivalent Phantoms using Fiber Bragg Gratings and Optical Coherence Tomography," Proc. of SPIE 8915, 1-10 (2013).
[13] Grall-Maës, E., "Use of the Kolmogorov-Smirnov test for gamma process," Journal of Risk and Reliability 226(6), 624-634 (2012).
[14] Walck, C., [Hand-book on Statistical Distribution for experimentalists], 69-143 (2007).
[15] Einstein, A., [Investigations on the Theory of the Brownian Movement], Courier Dover Publications, 1-2 (1956).
[16] Berne, B. J. and Pecora, R., [Dynamic Light Scattering With Applications to Chemistry, Biology, and Physics], Wiley-Interscience Publication, New York, London, Sydney and Toronto, 10-52 (1976).
[17] Farhat, G., Mariampillai, A., Yang, V. X. D., Czarnota, G. J. and Kolios, M. C., "Optical coherence tomography speckle decorrelation for detecting cell death," Proc. of SPIE 7907, 1-10 (2011).